Dynamic Catalyst Restructuring during Carbon Nanotube Growth

Michael Moseler,[†,‡,§,*] Felipe Cervantes-Sodi,[⊥,∥,*] Stephan Hofmann,[⊥] Gábor Csányi,[⊥] and Andrea C. Ferrari[⊥]

[†]Fraunhofer Institute for Mechanics of Material IWM, Freiburg, Germany, [‡]Department of Physics, University of Freiburg, Freiburg, Germany, [§]Freiburg Materials Research Center, Freiburg, Germany, [⊥]Department of Engineering, University of Cambridge, Cambridge, U.K., and [∥]Departamento de Física y Matemáticas, Universidad Iberoamericana, Lomas de Santa Fe, DF, Mexico

ABSTRACT We study the restructuring of solid nickel catalyst nanoparticles during carbon nanotube growth by environmental transmission electron microscopy and multiscale modeling. Our molecular dynamics/continuum transport calculations of surface-diffusion-mediated restructuring are in quantitative agreement with the experimentally observed catalyst shape evolutions. The restructuring time scale is determined by reduced Ni diffusion through the stepped Ni—C interface region where the catalyst surface strongly anchors to the growing nanotube.

KEYWORDS: carbon nanotube · catalysts · growth · atomic diffusion

Catalytic chemical vapor deposition (CVD) is one of the most promising techniques for both bulk production and deterministic growth on surfaces of carbon nanotubes (CNTs) and nanofibers (CNFs).[1−3] Transition metal catalyst particles are thereby exposed to a gaseous carbon precursor at elevated temperatures. For many catalyst−support systems, in particular for low temperature growth and processing, the catalyst remains in the solid state.[4−6] Environmental transmission electron microscopy (ETEM)[4,5,7−13] shows that the CNT/CNF morphology is governed by the dynamic reshaping of the catalyst particles. While specific changes in the catalyst faceting can influence the chirality,[14] or the graphene layer stacking in CNFs,[4] a much more pronounced catalyst elongation and contraction dynamics determines the growth mode and overall structure.[4,5] Such catalyst shape oscillations occur in the initial phases of tip and root growth[4,11] and during the formation of bamboo intersections.[4,5,10] A key requirement for deterministic growth is to understand and control the dynamic restructuring of the catalyst before and during feed-gas exposure.

Thermally induced shape fluctuations or adsorbate-induced restructuring of supported nanoparticles are well-known in heterogeneous catalysis[15,16] and are usually explained by surface diffusion and free-energy minimization.[17,18] Density functional calculations have shown that the CNT growth mechanism involves a low barrier Ni surface diffusion on Ni(111) with a graphene overlayer.[4] However, key to the understanding of CNT/CNF CVD are not individual diffusion barriers on specific facets, but rather the collective catalyst particle dynamics, particularly in response to the growing graphitic planes favoring the formation of Ni step edges.

In literature, the liquid-like shape changes of such confined particles are interpreted as plastic deformations induced by strong wall stresses,[8,9] or as surface melting,[19] or even as total melting,[20] caused by a melting point depression of finite-sized particles.[21] To the best of our knowledge, there is currently no convincing theoretical support for any of these interpretations. Most previous works focused either on low index surfaces[4,6] or on catalyst particles with a few tens of atoms.[22−25]

Here, we combine multiscale modeling with ETEM experiments in order to elucidate the mechanisms underlying the catalyst reshaping. Our classical MD simulations reveal that the solid Ni particles deform rapidly *via* capillary-driven surface diffusion on a crystalline core. This transport process is sometimes interrupted by collective slip events. There is no indication of Ni mass transport due to bulk diffusion, plastic deformation, or liquefaction. We present a continuum approach, based on surface diffusion between two curved Ni surfaces with different chemical potentials, able to predict Ni particle shape dynamics in quantitative agreement with the ETEM experiments.

*Address correspondence to michael.moseler@iwm.fraunhofer.de, felipe.cervantes@uia.mx.

Received for review August 23, 2010 and accepted October 29, 2010.

Published online November 9, 2010. 10.1021/nn102118y

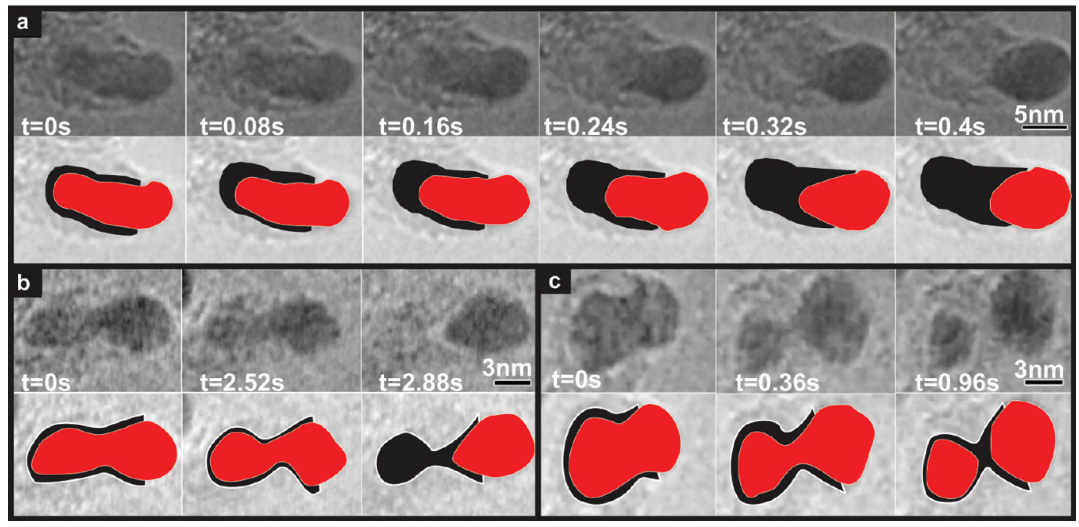

Figure 1. ETEM image sequences of the Ni particle at the tip of a growing CNF in 3:1 NH_3/C_2H_2 at 1.3 mbar and $T \sim 750$ K (movies in Supporting Information). The growth T refers to the thermocouple reading on the ETEM holder mini furnace. (a) Particle detaches from the internal confining carbon cap and relaxes from a strongly elongated shape to a spheroid within 400 ms. (b) An hourglass shaped carbon shell begins to form (left snapshot) leading to a neck in the middle of the particle (middle snapshot). The particle sometimes escapes the nanoconstriction (right snapshot, b), but often fractures (c).

We conclude that the dewetting dynamics is governed by a reduced Ni surface diffusion through stepped Ni−C interface regions where different Ni surfaces coincide.

RESULTS AND DISCUSSION

Figure 1 exemplifies three typical events occurring during CNF growth (see the Methods section for experimental details). Figure 1a displays the frequently observed elongation/contraction scenario.[4,5,7,9−11,13] The particle repeatedly contracts from an elongated to a spherical shape on a time scale of ~500 ms. Graphitic layers that constrict the catalyst particle in the radial direction can additionally influence the catalyst dynamics. Our ETEM data show that in some cases the catalytic particle is able to leap through these carbon nanoconstrictions (Figure 1b). However, the carbon constriction can also induce fracture, resulting in catalyst fragments buried inside a CNT bamboo section and a smaller catalyst particle that continues to catalyze further growth (Figure 1c). In agreement with previous ETEM experiments,[4,5,10] the catalyst particles show lattice fringes (see Supporting Information) indicating crystallinity at the given CVD conditions.

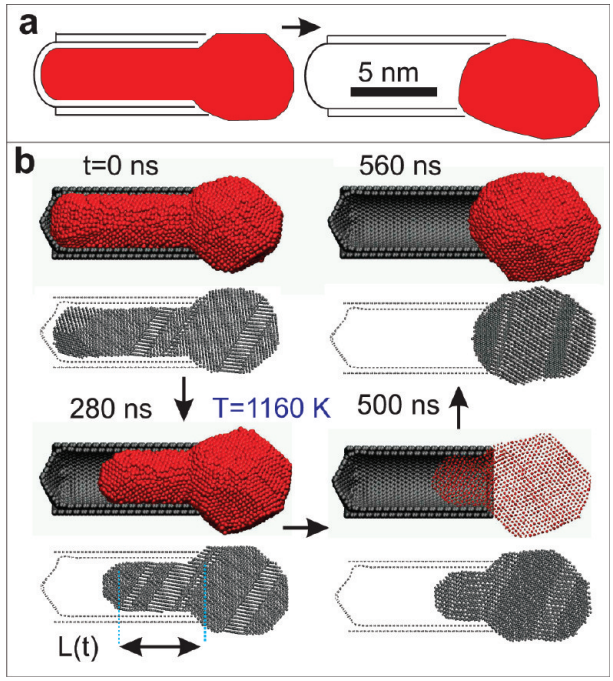

Figure 2. Molecular dynamics simulation of shape evolution for a solid Ni particle inside a double-walled CNT. (a) Sketches of ETEM images from ref 4. Ni is depicted in red and C in black. (b) Corresponding snapshots from a MD at 1160 K. The gray panels are cross sections of the relaxed structure, showing the evolution of grain boundaries. The apparent structural dynamics in the particle head is due to its slight rotation with respect to the CNT axis.

In the following, we rationalize the catalyst reshaping by the combination of molecular dynamics (MD) simulations and a continuum transport model.

We first consider the catalyst contraction depicted in Figure 1a. At $T = 750$ K, the Ni particle at the tip of a growing double-walled CNT detaches suddenly from the substrate (presumably due to passivation of the support or completion of a bamboo carbon membrane) and leaps outside the tube (see Figure 2a for an idealized sketch of TEM snapshots from ref 4). In ref 4, the reshaping occurred between two TEM frames, that is, within less than 0.5 s, and it was not possible to infer the precise transport mechanism from the image sequence. Here we combine the better temporal resolution of our experiments (Figure 1) with physical modeling to identify the relevant processes.

Classical MD simulations of a system with the same size as in ref 4 are performed: a Ni_{10561} particle in a double-walled (42,0)|(50,0) CNT, with a conical end-cap on one side, zigzag termination on the other (see Figure

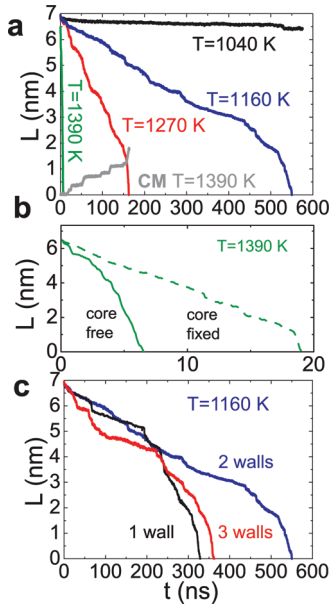

Figure 3. (a−c) Particle tail length evolution inside the CNT for different *T*. In (a), the gray curve labeled CM is the center of mass displacement of a core section initially located at the CNT exit. (b) Magnification of the 1390 K curve from (a) and corresponding curve for a particle with fixed Ni atoms in a cylindrical region of radius 0.3 nm and length 0.4 nm close to the CNT exit (fixed core). (c) Tail length evolution at *T* = 1160 K for 3 tubes with 1, 2, and 3 walls.

2b for the initial configuration), overall length of 12.8 nm, an initial head diameter of 4.8 nm, and tail diameter of 2.7 nm.

The forces on Ni atoms are derived from Ni−Ni tight-binding[26] and a density functional parametrized coordination-dependent Ni−C Morse potential (see the Methods section for details), with van der Waals bonding of Ni to CNT walls[4] and covalent bonding in the stepped Ni−C interface region. A fcc Ni external head and an internal tail inside the (50,0) tube are thermalized at 1390 K. The (42,0) tube is introduced by slowly moving C atoms from 3 Å outside the (50,0) tube to the final position mimicking the formation of an inner wall.[4,10] During this compression step and subsequent 10 ns thermalization at four temperatures (1040, 1160, 1270, 1390 K), the Ni interaction with the conical end-cap is covalent, anchoring the nanoparticle. At t = 0 ns, this is switched to van der Waals and the particle evolves freely. Figure 2b plots two sets of four snapshots of a T = 1160 K particle leaving the tube within 560 ns. Ni(111) and Ni(100) facets on the outside head and inside tail are seen during the whole trajectory, indicating solidity, despite reshaping (see Figure 2b, t = 280 ns). This is corroborated by the cross sections, showing crystalline order for all times and temperatures (Figure 2b), with few grain boundaries (mostly twins) from the initial compression.

Figure 3a shows the length evolution, $L(t)$, of the Ni tail inside the CNT. For the lowest temperature (black curve, T = 1040 K), the particle escapes the CNT with constant speed, resulting in a linear dependence of L on t, interrupted only once by a step at t = 530 ns. This happens also for higher T, but linear sections are more frequently interrupted by steps (see the red T = 1270 K curve in Figure 3a). During these, the crystalline core of the tail moves outward (the gray curve labeled CM in Figure 3a plots the evolution of its center of mass). Interestingly, if we freeze the initial position of a few Ni atoms at the tail center, close to the CNT exit, even for the highest T = 1390 K, a linear $L(t)$ dependence can be observed (Figure 3b). Figure 3c compares the length evolution of three systems: a single wall (black), a double wall (blue, also shown in Figure 3a), and a triple wall tube (red). Interestingly, as explained later, all three

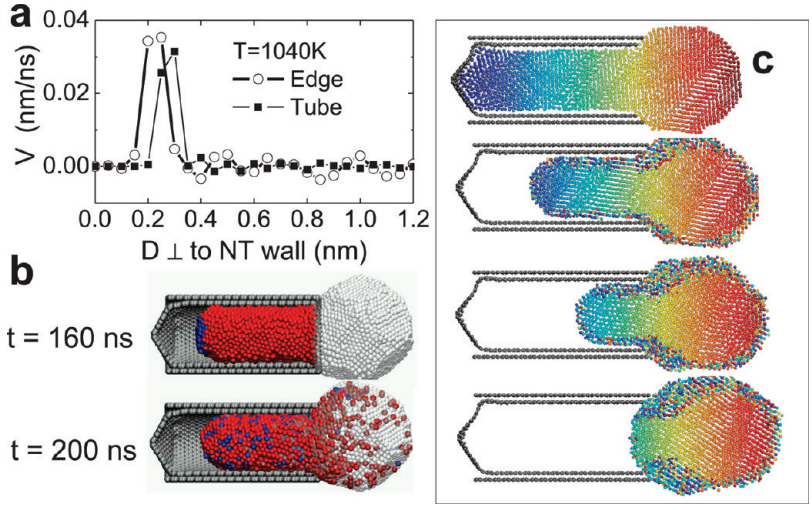

Figure 4. (a) Velocity component parallel to the CNT walls as a function of distance to the walls for Ni atoms inside the tube (solid squares) or at the CNT edge (open circles) at 1040 K. (b,c) Snapshots from the *T* = 1160 K trajectory. In (b), the Ni atoms are colored according to their location at *t* = 160 ns: the outer first layer of the tail is red, the rest is blue, while the outside head is white/gray. At *t* = 200 ns, many surface atoms have diffused outside. In (c), atoms are colored according to their position along the axis from left (blue) to right (red). Note that the positions in the internal part of the head hardly change.

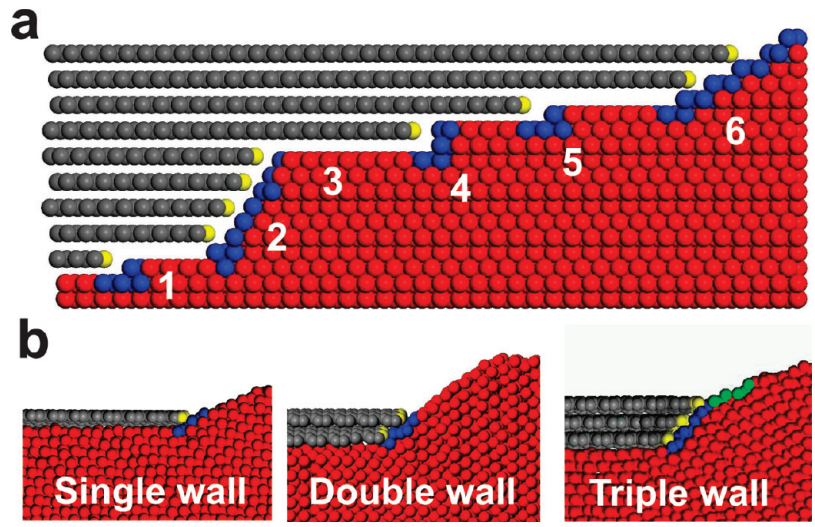

Figure 5. (a) Schematic model of catalyst (red and blue) cross section, highlighting the surface Ni atoms (blue) in contact with the edge C atoms (yellow) of a 9 wall CNT(gray). The 1−3 represent low index surfaces, 4 and 5 step edges, 6 an high index surface. Surfaces with equal Miller indices are linked by steps, surfaces with different Miller indices by kinks. The mobility of the diffusing Ni atoms is limited by the steps, kinks, and the high index surfaces. (b) Snapshots of the kink between the low index surfaces on the tail and head in single-, double-, and triple-wall CNT simulations. The triple-wall one with a second kink between the blue and green atoms.

cases present similar $L(t)$ curves with linear and stepped regions and the same order of magnitude in the overall evolution time.

We now focus on the basic transport mechanism. The average velocity profile in Figure 4a indicates that Ni transport remains limited to the close vicinity of the CNT walls. This is further confirmed by the snapshots in Figure 4b,c. In Figure 4b, the atom colors in the $T = 1160$ K particle are chosen according to their position at $t = 160$ ns. The outer Ni atom layer is plotted in red, while the remaining tail atoms are depicted in blue. At a later time (Figure 4b, $t = 200$ ns), a substantial number of outer layer atoms have moved outside the CNT, covering the head surface. The cross sections in Figure 4c are color-coded accordingly with the $t = 0$ ns atomic positions. These show that the particle core is unchanged during the entire simulation; that is, grain boundary motion cannot explain the Ni transport. This suggests that nanoparticles in CNTs can change shape quite efficiently by surface diffusion on a rigid metal core, resulting in the apparent liquid-like behavior. This diffusive transport competes with stochastic collective core motions reminiscent of stick−slip events in tribological systems.[27]

In experiments,[4,5,8] and in our MD model, the equilibrium contact angle of Ni on graphene, θ, is ∼180°, indicating that the particle does not wet the CNT. The chemical potential, $\mu_r = -2\gamma\Omega\cos(\theta)/r$, of Ni surface atoms on the half sphere (with radius $r = 1.35$ nm) at the end of the tail is higher than on the outer head of radius R, $\mu_R = 2\gamma\Omega/R$ (see Figure 6). Here, $\gamma \approx 22.78$ eV/nm^2 is the surface tension, and $\Omega = 0.011$ nm^3 the Ni atomic volume. This chemical potential gradient is the driving force for surface diffusion. A related Laplace pressure exerts an axial force $F = 2\gamma\pi r^2[-\cos(\theta)/r - 1/R]$ on the particle tail. This increases with time (since R increases) driving additional stick−slip events, especially at the end of our higher T simulations.

We now derive a continuum description of the diffusion-mediated transport process. Both Ni endcaps are interpreted as reservoirs with two chemical potentials, μ_r and μ_R. Their difference drives a surface diffusion current, following a Nernst−Einstein relation,[28] with an average velocity

$$v = \frac{\mu_R - \mu_r}{k_B T \int_{-L}^{0} \frac{dz}{D_s(T,z)}} \qquad (1)$$

along the encapsulated particle tail surface; k_B is the Boltzmann constant, $D_s(z)$ a surface diffusion coefficient with axial spatial dependence, which needs to be taken into account since the mobility of the Ni atoms depends strongly on the Ni surface orientations in different CNT sections and on variations in defect densities, such as steps and kinks, in the region connecting tail with head.

By equating the rate of transported volume, $2\pi r\rho_s\Omega v$, with the volume decrease of the tail, $-\pi r^2 dL/dt$, and using volume conservation, $4/3\pi R_f^3 = 4/3\pi R^3 + \pi r^2 L + 2/3\pi r^3$, we obtain an equation of motion for the tail length:

$$\frac{dL}{dt} = -\frac{4}{r^2}\frac{\gamma\Omega^2\rho_s}{k_B T \int_{-L}^{0} \frac{dz}{D_s(T,z)}}\left[-\cos\theta - \frac{r}{R(L)}\right] \qquad (2)$$

where $\rho_s = 18.6$ nm^{-2} is the diffusing atoms areal density, $R(L) \approx (R_f^3 - r^3/2 - 4Lr^2/4)^{1/3}$, the outer head radius, and $R_f = 3.05$ nm the particle radius after complete expulsion.

In the most general case, D_s is determined by several different processes (see Figure 5a for a schematic representation of the Ni surface), including diffusion on high and low index surfaces (*e.g.*, 5 and 6 in Figure 5a), across kinks between these surfaces (*e.g.*, between 1 and 2 or 2 and 3 in Figure 5a), and over step edges (*e.g.*, steps 4 and 5 in Figure 5a). The Ni tail surface structure inside the tube is very regular, consisting mainly of low index surfaces and no steps and kinks. We expect the average surface diffusion coefficient D_s^{tube} in this zone to be high. On the other hand, the steps and kinks in the exit region and the strong C−Ni interaction at the CNT edges slow diffusion, leading to a small average diffusion coefficient D_s^{exit}. With this in mind, we decompose the integral $\int_L^0(dz)/(D_s(T,z))$ into two parts, one for fast intratube diffusion and one for slow exit diffusion:

$$\frac{dL}{dt} = -\frac{4}{r^2}\frac{\gamma\Omega^2\rho_s}{k_BT\left(\frac{L-L_{exit}}{D_s^{tube}(T)}+\frac{L_{exit}}{D_s^{exit}(T)}\right)}\left[-\cos\theta - \frac{r}{R(L)}\right] \quad (3)$$

We calculate the intratube surface diffusion coefficient $D_s^{tube}(T)$ with MD for several temperatures by applying an external drift force f to a Ni cylinder of radius $r = 1.35$ nm inside a (42,0) CNT (see inset in Figure 7a). The applied chemical potential gradient $d\mu/dz = f = 0.1$ eV/nm is chosen in the order of magnitude of the force an atom on the particle surface would experience due to the difference in chemical potential between μ_r and μ_R. Note that, similar to our transient dewetting simulations, only the first outer layer shows significant drift. The diffusion coefficients can be calculated from the effective drift speed v of the first outer layer using (eq 1): $D_s^{tube} = vk_BT/(d\mu/dz)$. The results (red squares in Figure 7a) can be fitted by a bi-Arrhenius law

$$D_s^{tube}(T) = 13.63\times10^3\frac{nm^2}{ns}e^{-1.02eV/(k_BT)} + 8.90\times10^{17}\frac{nm^2}{ns}e^{-4.62eV/(k_BT)}$$

The fitted barriers differ substantially from the low 0.1 eV barrier calculated for the diffusion of Ni on Ni(111).[4,6] On the other hand, a bi-Arrhenius behavior with high barriers has been observed for surface diffusion experiments on Ni surfaces at higher temperatures.[29] It is well-known[30] that activation energies of dilute single atom diffusion differ substantially from more collective higher temperature diffusion. Nevertheless, in both regimes, the migration on extended low index facets is fast; therefore, D_s^{tube} is high for Ni(111)and Ni(110).[29]

A continuum model based solely on surface diffusion along the cylindrical tail (using our calculated D_s^{tube} in eq 3, assuming $D_s^{exit} = 0$) would overestimate the particle speed. For example, at $T = 1160$ K, the particle would leave the tube within 80 ns in contradiction to our MD simulations. Even at $T = 750$ K, the particle would only need 13 μs, while our experimental time scale is 0.5 s. This discrepancy results from neglecting the reduced surface diffusion in the exit zone. In our MD models, the Ni atoms experience two different diffusion processes. First, they diffuse on low index facets on the intratube tail. Second, they pass a kink where the particle tail converts into the head. Once the Ni atoms pass the kink, they are already outside the tube. We consider here a special case since our model only has one kink and no steps and a very short exit region of length $L^{exit} \approx 0.5$ nm. For CNTs and CNFs with many walls (shown in the atomistic sketch of Figure 5a), the appearance of extra kinks and additional steps results in a different average D_s^{exit} and larger L_{exit}, slowing the dewetting rate. Thus, in our model, the kink region dominates transport. However, there is no simple way to calculate D_s^{exit} using the drift force method in a peri-

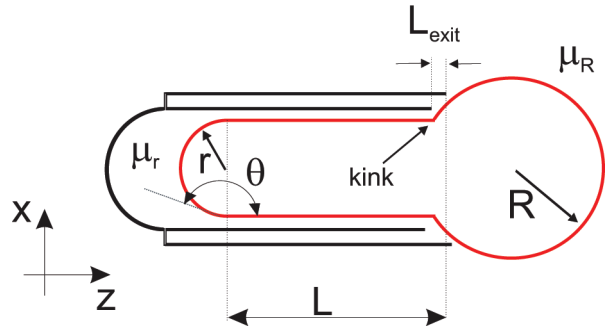

Figure 6. Continuum model: spherical caps with radii r, R and chemical potentials μ_r, μ_R, exchange atoms by surface diffusion along the particle tail of length L, and a short cone-shaped section of length L_{exit}. Head and tail are joined in the kink region; θ is the contact angle between Ni and CNT.

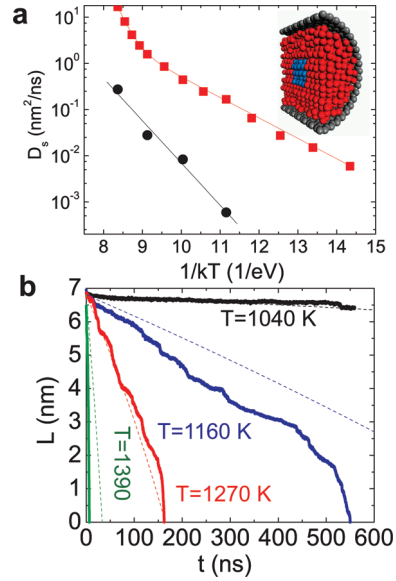

Figure 7. (a) Arrhenius plot of surface diffusion inside the CNT (red squares) and at the exit (black dots). The inset shows the axially periodic structure (2.98 nm periodicity) used to calculate diffusion. The blue atoms in a cylindrical region of 1 nm diameter and length are fixed to avoid tail slip during the 20 ns MD. Red atoms can diffuse. (b) Comparison between L evolution described by the continuum model (dashed lines) and by transient MD (solid lines) for different T.

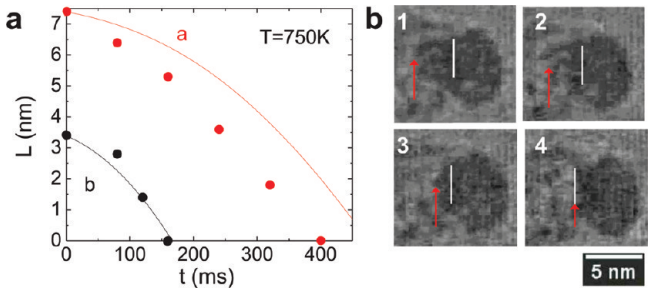

Figure 8. (a) Comparison between experimental ETEM data and our continuum model. Red dots correspond to Figure 1a and black dots to the ETEM sequence in (b). Vertical bars in (b) mark the extension of the catalysts tail. We roughly estimate the uncertainty for the visual interpretation and extraction of the tail length from the experimental ETEM image sequences to be on the order of 1 nm.

odic system. We estimate D_s^{exit} from our transient $L(t)$ curves in Figure 3a by inverting eq 3 for small times. The slopes $dL/dt(t = 0)$ and L_{exit} =0.5 nm are then used to calculate D_s^{exit}. Note that the slip contribution to $L(t)$ in Figure 3a is now eliminated. The resulting D_s^{exit} (black dots, Figure 7a) is much smaller than D_s^{tube} and is also fit by an Arrhenius law (black line, Figure 7a), $D_s^{exit}(T) = 10.12 \times 10^6$ nm^2/ns(exp[-2.11eV/(k_BT)]) .

We now discuss the origin of this strongly reduced diffusivity. Before leaving the CNT, the diffusing Ni atoms on the low index facets inside the CNT have to pass through a kink where they are temporarily higher coordinated. In order to hop from the kink to a surface on the outer Ni head, an energy $E_B > 1.3$ eV has to be invested.[31] Note, that this E_B represents an energetic barrier that has the same order of magnitude as the 2.1 eV in our Arrhenius fit.

Additional dewetting simulations with a single-wall and a triple-wall tube, at $T = 1160$ K, show that the drift velocity in the exit area hardly depends on the number of walls (Figure 3c). The quantity D_s^{exit}/L_{exit} for 1, 2, and 3 walls is 0.015, 0.016, and 0.012 nm/ns, respectively. For the single- and the double-wall simulations, the catalyst structure at the exit is identical; that is, no additional kinks or steps are generated if slightly longer outer CNT walls are added (Figure 5b). The triple-wall simulation often shows two kinks and some areas of high index surfaces between the kinks. One of the kinks defines the boundary between the tail and the head of the particle (as in the single- and double-wall cases) and is always present. The second kink appears in the outer part of the particle. In Figure 5b, the common kinks for the single-, double-, and triple-wall simulations are localized at the left side of the blue atoms. The exclusive kink of the triple-wall simulation is localized between the blue and green atoms. The existence of kinks and high index surfaces between the kinks can be incorporated in our model by decomposing D_s^{exit}/L_{exit} into a kink and a high index surface contribution $L_{exit}/D_s^{exit} = L_{kink}/D_s^{kink} + L_{hi}/D_s^{hi}$.

Using $D_s^{tube}(T)$ and $D_s^{exit}(T)$ in eq 3 provides continuum estimates for the $L(t)$ curves in good agreement with MD (compare dashed lines with solid lines in Figure 7b). This close correspondence between atomistic and continuum description encourages us to compare the diffusion model predictions with the experimentally observed tail length evolution. From eq 3, $L(t)$ is calculated for the particle in Figure 1a using $T = 750$ K, $r = 2.4$ nm, $R_f = 3.8$ nm, and $L(0) = 7.4$ nm. Figure 8a shows the theoretical result (red line) along with the corresponding $L(t)$ extracted from Figure 1a (red dots).

The continuum model reproduces the experimental shape dynamics extremely well. The predicted 480 ms dewetting time is on the same order of magnitude as the measured 400 ms. The general shape of the experimental and theoretical $L(t)$ curves is identical. We analyzed other elongation/contraction events in the same way to verify that the close agreement between experiment and theory is not accidental. Black dots in Figure 8a show the shape evolution of a particle with smaller tail (see Figure 8b). Also, in this case, the continuum model with $r = 2$ nm, $R_f = 2.9$ nm, and $L(0) = 3.4$ nm (black curve) agrees well with the experiment (black dots).

We note that the comparison with the experiment is based on the following implicit assumptions: (a) the structure of the experimental catalyst at the exit is identical to that of our double-wall simulation (*i.e.*, the L_{exit}/D_s^{exit} from our simulation can be used), (b) the negligibility of dissolved C in the metal particle, and (c) the applicability of the Arrhenius law $D_s^{exit}(T)$ for $T < 1000$ *K*. Assumption (a) is motivated by the fact that in the experiments CNFs with a L_{exit} similar to our atomistic model were considered.[4,5] Assumption (b) is justified by additional simulations presented in the Supporting Information. Assumption (c) is the most critical because it indicates that the diffusion processes remain unchanged if temperature is lowered by 300 K (*i.e.*, a possible bi-Arrhenius behavior is excluded). Despite these assumptions, we believe that our continuum model (eq 2) can be used as a predictive tool once the experimental $D_s^{exit}(T)$ is accessible.

We now discuss some implications of eq 2. We start with the influence of the contact angle θ. For the comparison with the ETEM, we assumed a complete dewetting of the catalyst in the bamboo compartments (*i.e.*, $\theta = 180°$). However, a high C vacancy density in the growing CNT will result in contact angles $\theta < 180°$, reducing the capillary driving force in eq 2. This will slow down the elongation/contraction dynamics and, in the worst case, θ can drop below a critical angle, $\theta_c = \arccos(r/R)$, such that eq 2 predicts an inward motion of the catalyst resulting in particle overgrowth, in agreement with what experimentally observed in refs 32 and 33.

In general, it is reasonable to assume that the C vacancy density close to the catalyst/CNT interface is initially high and decreases with time while new C arrives

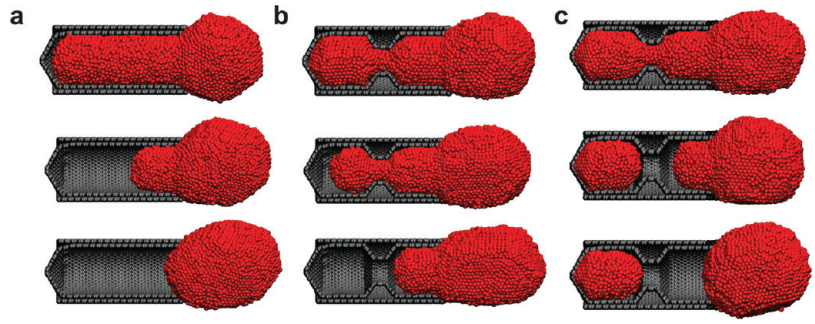

Figure 9. Nanoparticle reshaping at $T = 1390$ K. (a) Leap-frog in a double-walled CNT, and (b) through a neck in the inner wall. (c) Fracture caused by a Nichols-Mullins instability[34] initiated by a constriction in the CNT. In (a,b), the particle is free to evolve, while it is anchored at the back of the CNT in (c). Corresponding MD movies in Supporting Information.

from the catalyst. This implies that the contact angle $\theta(z)$ depends on the distance z from the tube exit, increasing from $\theta \approx 0°$ in the tube exit region to $\theta = 180°$ far away from the growth zone. In order to avoid the elongation/contraction dynamics and grow ideal CNTs, the rate R_v for vacancy filling (which is related to C transport) has to be large enough such that $\theta(z) < \theta_c$ only in the vicinity of the tube exit. If R_v decreases, the tube section with $\theta(z) < \theta_c$ increases and the particle tail inside the tube gets longer. For such long tails, there is a considerable chance for the addition of a new inner wall resulting in a bamboo compartment[10] and the initiation of an elongation/contraction cycle. In this case, the bamboo cap heals *after* the formation of a defect-free side wall with $\theta = 180°$. Since the walls continue to grow, the nanoparticle elongates until θ at the cap exceeds a critical angle, θ_c. This initiates the contraction phase of an elongation/contraction cycle. The tail length shrinks until it finds a new section with $\theta < \theta_c$ (usually close to the CNT exit).

The diffusion coefficient $D_s(T, z)$ is another crucial quantity for the elongation/contraction dynamics. As discussed above, the diffusion over steps, through kinks and on high index surfaces, dominates the Ni mobility (see Figure 5). Therefore, the integral entering eq 2 is approximated by

$$\int_{-L}^{0} \frac{dz}{D_s(T,z)} = \frac{L - L_{kink} - L_{step} - L_{hi}}{D_s^{tube}(T)} + \frac{L_{kink}}{D_s^{kink}(T)} + \frac{L_{step}}{D_s^{step}(T)} + \frac{L_{hi}}{D_s^{hi}(T)} \quad (4)$$

Here L_{kink}, L_{step}, and L_{hi} denote the total lengths of kinked, stepped, and high index zones, and D_s^{kink}, D_s^{step}, and D_s^{hi} are the corresponding average diffusion coefficients. Figure 5b shows that for nanoparticles in few-walled CNTs only one kink and no steps are present; therefore, Ni diffusion should not dominate the growth at $T \geq 750$ K because the contractions predicted by our model are rather fast. However, in the case of few-walled tubes at even lower temperatures, the contraction dynamics can be so slow that the catalyst gets encapsulated in the tube. The same might happen for multiwalled CNTs whose walls do not grow at the same rate. In this case, a region with many kinks, steps, and high index facets may give a strongly reduced diffusion and early catalyst encapsulation. Thus, multiwalled CNTs whose walls grow at the same speed and whose edges are arranged so regularly that the neighboring Ni can form low index surfaces have the highest chance to avoid encapsulation.

We now discuss the other reshaping events in Figure 1. Additional MD simulations show that catalyst contraction is not restricted to straight tubes (Figure 9a). It also occurs in tubes with a neck shaped constriction (*e.g.*, a growing bamboo shell) although with a slightly reduced speed (Figure 9b). In agreement with our previous discussion, we find complete particle expulsion only when the anchoring forces inside the CNT become small enough, either by substrate passivation,[4] by complete closure of a bamboo cap,[10] or by sufficient reduction of CNT wall defects (increasing the contact angle above θ_c). If anchoring persists, the particle in the narrow constriction fractures (Figure 9c), similarly to the ETEM sequence in Figure 1c. This behavior can be interpreted as a Nichols-Mullins[34] instability driven by the high chemical potential in the neck region, resulting in a diffusion current out of the constricted zone, leading to shrinkage of the Ni particle neck in favor of the outside head. Even if one could be tempted to interpret the events in Figure 1 using fluidic concepts, the MD simulations in Figure 9 reveal that the nanoparticles remain solid during its whole shape evolution process.

A concurrent simulation of both the catalyst as well as the carbon diffusion would be necessary to fully understand the nanotube growth. Although some progress in the quantum chemical treatment of this problem can be expected, useful time scales for the catalyst and carbon dynamics are unlikely to be reached with electronic structure based methods within the next decade. Therefore, reliable classical carbon−nickel (or C−Fe) potentials allowing for a faithful description of the catalyst−carbon chemistry have to be developed.

Ordinary or time-accelerated molecular dynamics calculations based on such potentials will elucidate details of the structural evolution of the stepped catalyst−carbon interface at the tube exit. On the basis of such simulations, concepts have to be developed on how to control the dynamics in this interface area to achieve a steady state balance between carbon inflow and catalyst outflow. In addition, a deeper understanding of CNT defect healing will be crucial to avoid catalyst anchoring and thus elongation/contraction cycles. Such insights into the underlying atomic scale mechanisms will be useful to find optimum catalyst materials (*e.g.*, binary alloys) and catalyst diameters (*e.g.*, by using size selected soft-landed clusters) that stabilize a beneficial step structure at the CNT exit, therefore acting as custom tailored templates for a desired CNT chirality.

CONCLUSIONS

We explored the complex reshaping behavior of catalysts in growing nanotubes and nanofibers. We find that capillary-driven surface diffusion is the dominant transport mechanism, featuring a fast collective diffusion on the catalyst inside the tube and a strongly reduced Ni surface mobility through kinks and over steps in the Ni−C interface region.

METHODS

ETEM Measurements. We use a modified Tecnai F20 ETEM, operated at 200 kV, equipped with a differential pumping system and a Gatan imaging filter. The microscope permits pressures up to 10 mbar, with an information limit of 0.134 nm. Thin Ni films (99.9% purity) are thermally evaporated (base pressure $\sim 10^{-6}$ mbar) onto perforated SiO_x membranes (SPI supplies) or onto 2000 mesh Cu TEM grids (Agar Scientific) coated with SiO_x nanopowder (Degussa Aerosil Ox50) and a ~30 nm sputtered SiO_x layer. The samples are transferred in air to the ETEM. Growth conditions for Figure 1 are 3:1 NH_3/C_2H_2, 1.3 mbar, ~750K. Temperatures are measured by a thermocouple on the TEM holder mini furnace.

Molecular Dynamics. The Ni particle inside the static CNT is simulated by Langevin molecular dynamics[35] using the ATOMISTICA MD code (www.atomistica.de). Intrametallic Ni−Ni forces are derived from an established second moment tight-binding potential.[26] The Ni−C interaction at the ideal CNT wall is modeled by a Morse potential with fitted parameters from DFT using the local density approximation (LDA) as implemented in the CASTEP code.[36] We use ultrasoft pseudopotentials[36] with cutoff energy of 360 eV. The supercells consist of a trilayer Ni(111) slab and a pristine graphene layer (similar to refs 4, 37, and 38). The Brillouin zone (BZ) is sampled by Monkhorst-Pack grids of the form $P \times P \times 1$ with P such that the maximum spacing between k-points in the periodic directions is <0.1 Å^{-1}. We find that, to simulate the slab, the perpendicular distance between adjacent supercells needs to be 14 Å. The distance between the Ni(111) surface and the graphene is varied from 1.5 to 6 Å, and a Ni−C Morse potential is fitted to the resulting energy−distance curve. Our parameters for the Morse potential are $D = 0.0048$ eV, $r_0 = 3.61$ Å, $\alpha = 1.13$ Å^{-1}, indicating a van der Waals type bonding. We also tested the Ni (001)−graphene system because it has been reported that a single C atom is strongly attracted to the Ni(001) surface.[24] For the graphene Ni(001) interaction, our Morse parameters are close to the Ni(111) case: $D = 0.007$ eV, $r_0 = 3.11$ Å, $\alpha = 1.012$ Å^{-1}, indicating that Ni low index surfaces interact weakly with ideal graphene and CNTs.

Also for Ni at CNT edges, a Morse potential is used. Its parameters are estimated from DFT calculations of a Ni(111) step surface interacting with a zigzag graphene strip. In this case, Morse parameters $D = 0.3$ eV, $r_0 = 2$ Å, $\alpha = 2$ Å^{-1} are chosen. This more covalent type of interaction has to be restricted to Ni with a Ni coordination number between 6 and 8. The Ni−C interaction for Ni atoms with coordination higher than 9 or lower than 6 are kept van der Waals-like in order to reproduce the structure of the CNT−Ni interface at the CNT edges known from ETEM studies.[5]

Acknowledgment. M.M. thanks the University of Cambridge for the hospitality during a sabbatical funded by the Fraunhofer society and for funding from BMBF CaNaMAT, DFG priority program SPP1153 and Landesstiftung Baden-Württemberg. F.C.S. acknowledges funding from conacyt Mexico, S.H. from the Royal Society and Peterhouse, A.C.F. from the European Research Council Grant NANOPOTS, and a Royal Society Brian Mercer Award for Innovation. A.C.F. is a Royal Society Wolfson Research Merit Award holder. We thank R. Sharma, G. Du, and K. Weiss for help with ETEM microscopy, R. Dunin-Borkowski for assistance with ETEM video processing, and A. Klemenz for the contact angle of Ni on graphene. Computations were performed on the Fraunhofer clusters O1 and JOE, on the Cambridge HPCF, and the Research Center for Scientific Simulations of the University of Ioannina.

Supporting Information Available: Additional details and information relative to the solid state of the catalyst (ETEM snapshots of a Ni nanocrystal, and the effect of dissolved C in the nanoparticle). Real time ETEM movies and MD simulations of Ni nanoparticles dewetting from CNT *via* surface diffusion. This material is available free of charge *via* the Internet at http://pubs.acs.org.

REFERENCES AND NOTES

1. Radushkevich, L.; Lukyanovich, V. O. Strukture Ugleroda, Obrazujucegosja Pri Termiceskom Razlozenii Okisi Ugleroda na Zeleznom Kontakte. *Z. Fisic. Chim.* **1952**, *26*, 88–95.
2. Dai, H.; Rinzler, A.; Nikolaev, P.; Thess, A.; Colbert, D. T.; Smalley, R. E. Single-Wall Nanotubes Produced by Metal-Catalyzed Disproportionation of Carbon Monoxide. *Chem. Phys. Lett.* **1996**, *260*, 471–475.
3. Hata, K.; Futaba, D.; Mizuno, K.; Namai, T.; Yumura, M.; Iijima, S. Water-Assisted Highly Efficient Synthesis of Impurity-Free Single-Walled Carbon Nanotubes. *Science* **2004**, *306*, 1362–1364.
4. Helveg, S.; Lopez-Cartes, C.; Sehested, J.; Hansen, P. L.; Clausen, B. S.; Rostrup-Nielsen, J. R.; Abild-Pedersen, F.; Norskov, J. K. Atomic-Scale Imaging of Carbon Nanofibre Growth. *Nature* **2004**, *427*, 426–429.
5. Hofmann, S.; Sharma, R.; Ducati, C.; Du, G.; Mattevi, C.; Cepek, C.; Cantoro, M.; Pisana, S.; Parvez, A.; Cervantes-Sodi, F.; *et al. In Situ* Observations of Catalyst Dynamics during Surface-Bound Carbon Nanotube Nucleation. *Nano Lett.* **2007**, *7*, 602–608.
6. Hofmann, S.; Csányi, G.; Ferrari, A. C.; Payne, M. C.; Robertson, J. Surface Diffusion: The Low Activation Energy Path for Nanotube Growth. *Phys. Rev. Lett.* **2005**, *95*, 036101.
7. Jensen, K.; Mickelson, W.; Han, W.; Zettl, A. Current-Controlled Nanotube Growth and Zone Refinement. *Appl. Phys. Lett.* **2005**, *86*, 173107.
8. Sun, L.; Banhart, F.; Krasheninnikov, A. V.; Rodriguez-Manzo, J. A.; Terrones, M.; Ajayan, P. M. Carbon Nanotubes as High-Pressure Cylinders and Nanoextruders. *Science* **2006**, *312*, 1199–1202.

9. Rodriguez-Manzo, J. A.; Terrones, M.; Terrones, H.; Kroto, H. W.; Sun, L.; Banhart, F. *In Situ* Nucleation of Carbon Nanotubes by the Injection of Carbon Atoms into Metal Particles. *Nat. Nanotechnol.* **2007**, *2*, 307–311.
10. Lin, M.; Tan, J. P. Y.; Boothroyd, C.; Loh, K. P.; Tok, E. S.; Foo, Y.-L. Dynamical Observation of Bamboo-like Carbon Nanotube Growth. *Nano Lett.* **2007**, *7*, 2234–2238.
11. Yoshida, H.; Takeda, S.; Uchiyama, T.; Kohno, H.; Homma, Y. Atomic-Scale *In-Situ* Observation of Carbon Nanotube Growth from Solid State Iron Carbide Nanoparticles. *Nano Lett.* **2008**, *8*, 2082–2086.
12. Jin, C.; Suegana, K.; Iijima, S. Plumbing Carbon Nanotubes. *Nat. Nanotechnol.* **2008**, *3*, 17–21.
13. Rodriguez-Manzo, J.; Janowska, I.; Pham-Huu, C.; Tolvanen, A.; Krasheninnikov, A.; Nordlund, K.; Banhart, F. Growth of Single-Walled Carbon Nanotubes from Sharp Metal Tips. *Small* **2009**, *5*, 2710–2715.
14. Zhu, H.; Suenaga, K.; Wei, J.; Wang, K.; Wu, D. A Strategy To Control the Chirality of Single-Walled Carbon Nanotubes. *J. Cryst. Growth* **2008**, *310*, 5473–5476.
15. Somorjai, G.; Hove, M. V. Adsorbate-Induced Restructuring of Surfaces. *Prog. Surf. Sci.* **1989**, *30*, 201–231.
16. Hansen, P. L.; Wagner, J. B.; Helveg, S.; Rostrup-Nielsen, J. R.; Clausen, B. S.; Topsoe, H. Atom-Resolved Imaging of Dynamic Shape Changes in Supported Copper Nanocrystals. *Science* **2002**, *295*, 2053–2055.
17. Eggers, J. Coalescence of Spheres by Surface Diffusion. *Phys. Rev. Lett.* **1998**, *80*, 2634.
18. Chung, J. Y.; Nolte, A. J.; Stafford, C. M. Diffusion-Controlled, Self-Organized Growth of Symmetric Wrinkling Patterns. *Adv. Mater.* **2009**, *21*, 1358–1362.
19. Larouche, F.; Smiljanic, O.; Sun, X.; Stansfield, B. Solutal Benard-Marangoni Instability as a Growth Mechanism for Single-Walled Carbon Nanotubes. *Carbon* **2005**, *43*, 986–993.
20. Harutyunyan, A. R.; Tokune, T.; Mora, E. Liquid as a Required Catalyst Phase for Carbon Single-Walled Nanotube Growth. *Appl. Phys. Lett.* **2005**, *87*, 051919.
21. Schmidt, M.; Kusche, R.; Issendorff, B.; Haberland, H. Irregular Variations in The Melting Point of Size-Selected Atomic Clusters. *Nature* **1998**, *393*, 238–240.
22. Shibuta, Y.; Maruyama, S. Molecular Dynamics Simulation of Formation Process of Single-Walled Carbon Nanotubes by CCVD Method. *Chem. Phys. Lett.* **2003**, *382*, 381–386.
23. Gavillet, J.; Loiseau, A.; Journet, C.; Willaime, F.; Ducastelle, F.; Charlier, J.-C. Root-Growth Mechanism for Single-Wall Carbon Nanotubes. *Phys. Rev. Lett.* **2001**, *87*, 275504.
24. Borjesson, A.; Zhu, W.; Amara, H.; Bichara, C.; Bolton, K. Computational Studies of Metal−Carbon Nanotube Interfaces for Regrowth and Electronic Transport. *Nano Lett.* **2009**, *9*, 1117–1120.
25. Cervantes-Sodi, F.; McNicholas, T. P.; Simmons, J. G.; Liu, J.; Csányi, G.; Ferrari, A. C.; Curtarolo, S. Viscous State Effect on the Activity of Fe Nanocatalysts. *ACS Nano* **2010**, doi: 10.1021/nn101883s.
26. Rapallo, A.; Rossi, G.; Ferrando, R.; Fortunelli, A.; Curley, B. C.; Lloyd, L. D.; Tarbuck, G. M.; Johnston, R. L. Global Optimization of Bimetallic Cluster Structures. I. Size-Mismatched Ag−Cu, Ag−Ni, and Au−Cu Systems. *J. Chem. Phys.* **2005**, *122*, 194308.
27. Bhushan, B.; Israelachvili, J.; Landman, U. Nanotribology-Friction, Wear and Lubrication at the Atomic-Scale. *Nature* **1995**, *374*, 607–616.
28. Mullins, W. W. Theory of Thermal Grooving. *J. Appl. Phys.* **1957**, *28*, 333–339.
29. Bonzel, H.; Latta, E. Surface Self-Diffusion on Ni(110)-Temperature Dependence and Directional Anisotropy. *Surf. Sci.* **1978**, *76*, 275–295.
30. Naumovets, A. Collective Surface Diffusion: An Experimentalist's View. *Physica A* **2005**, *357*, 189–215.
31. Liu, C. L.; Adams, J. B. Diffusion Mechanisms on Ni Surfaces. *Surf. Sci.* **1992**, *265*, 262–272.
32. Marmur, A. Penetration of a Small Drop into a Capillary. *J. Colloid Interface Sci.* **1988**, *122*, 209–219.
33. Schebarchov, D.; Hendy, S. C. Capillary Absorption of Metal Nanodroplets by Single-Wall Carbon Nanotubes. *Nano Lett.* **2008**, *8*, 2253–2257.
34. Nichols, F. A.; Mullins, W. W. Surface (Interface) and Volume Diffusion Contributions to Morphological Changes Driven by Capillarity. *Trans. AIME* **1965**, *233*, 1840–1849.
35. Moseler, M.; Nordiek, J.; Haberland, H. On the Origin of Surface Smoothing by Energetic Cluster Impact: Molecular Dynamics Simulation and Mesoscopic Modeling. *Phys. Rev. B* **1997**, *56*, 15439.
36. Segall, M.; Lindan, P.; Probert, M.; Pickard, C.; Hasnip, P.; Clark, S.; Payne, M. First-Principles Simulation: Ideas, Illustrations and the CASTEP Code. *J. Phys.: Condens. Matter.* **2002**, *14*, 2717–2744.
37. Abild-Pedersen, F.; Norskov, J. K.; Rostrup-Nielsen, J. R.; Sehested, J.; Helveg, S. Mechanisms for Catalytic Carbon Nanofiber Growth Studied by *Ab Initio* Density Functional Theory Calculations. *Phys. Rev. B* **2006**, *73*, 115419.
38. Fuentes-Cabrera, M.; Baskes, M. I.; Melechko, A. V.; Simpson, M. L. Bridge Structure for the Graphene/Ni(111) System: A First Principles Study. *Phys. Rev. B* **2008**, *77*, 035405.